Progress In Electromagnetics Research, Vol. 177, 21–32, 2023

Highly Sensitive Temperature Sensing via Photonic Spin Hall Effect

Shuaijie Yuan[1], Jin Yang[1], Yong Wang[1], Yu Chen[2, *], and Xinxing Zhou[1, *]

Abstract—In this work, we propose a highly sensitive temperature sensor based on photonic spin Hall effect (PSHE). We find that, by involving the liquid crystal (LC) material, the spin spatial and angular shifts in PSHE are very sensitive to the tiny perturbation of temperature when the incident angle of light beam is near the Brewster and critical angles. Importantly, the phase transition from liquid crystal state to liquid state across the clearing point (CP) will lead to the transition of strong spin-orbit interaction to the weak one. During this process, we reveal that the sensitivity of our designed temperature sensor can reach a giant value with 8.27 cm/K which is one order of magnitude improvement compared with the previous Goos-Hänchen effect-based temperature sensor. This work provides an effective method for precisely determining the position of CP and actively manipulating the spin-orbit interaction.

1. INTRODUCTION

As a bridge for human's perceiving natural environment parameters, sensors have always been in a high development position. Among them, temperature sensor takes a great part. With the demand for higher sensitivity, a variety of temperature sensing technologies have emerged. Recently, optical temperature sensing has received a lot of attention due to its excellent antijamming capability and high accuracy, which is attributed to non-contact characteristics and the low loss propagation of light. The corresponding physical mechanism is to indirectly characterize temperature by detecting the optical behavior of temperature-controlled materials, such as optical fiber temperature sensor [1–6], liquid crystal temperature sensor [7–10], Goos-Hänchen effect-based temperature sensor [11], and Imbert-Fedorov effect-based temperature sensor [12]. In 2003, the influence of temperature on the surface plasmon response in metal materials [13] was revealed. Then temperature sensors based on Goos-Hänchen shifts [14] and composite Goos-Hänchen shifts [15] have been explored, which has greatly improved the sensitivity to 402 nm/K and 0.79 cm/K. However, it is still highly desirable to explore other kinds of simple and effective methods for enhancing the sensitivity of temperature sensor.

In this work, we propose a highly sensitive temperature sensing method based on photonic spin Hall effect (PSHE). The PSHE manifests itself as the spin-dependent splitting of left- and right-handed circularly polarized components of the reflected or transmitted light beam [16–22], which is different from the Goos-Hänchen effect. The physical mechanism is due to the spin-orbit interaction of light [23–29]. Importantly, the PSHE can precisely characterize the material properties, which makes it widely used in precise metrology [30–34], optical sensing [35–38], and spin-based nanophotonic devices [39–44]. In this model, we introduce the liquid crystal (LC) material which is very sensitive to the variation of temperature. Here, the PSHE in LC material can be an effective observable for precisely determining the change of temperature. We also find that the spin shifts in PSHE can experience a giant variation when

Received 29 January 2023, Accepted 14 March 2023, Scheduled 23 March 2023

* Corresponding authors: Yu Chen (yuchen@szu.edu.cn), Xinxing Zhou (xinxingzhou@hunnu.edu.cn).

[1] Key Laboratory of Low-Dimensional Quantum Structures and Quantum Control of Ministry of Education, Synergetic Innovation Center for Quantum Effects and Applications, School of Physics and Electronics, Hunan Normal University, Changsha 410081, China. [2] International Collaborative Laboratory of 2D Materials for Optoelectronics Science and Technology, Engineering Technology Research Center for 2D Material Information Function Devices and Systems of Guangdong Province, Institute of Microscale Optoelectronics, Shenzhen University, Shenzhen 518060, China.

the LC material changes from liquid crystal state to liquid state across the clearing point (CP). Based on this, we can achieve an optical temperature sensor with ultra-high sensitivity, and the position of CP can also be precisely revealed. Moreover, we can also efficiently obtain highly sensitive temperature sensing relatively far away from the CP temperature by choosing the incident angle of light beam as that near the Brewster and critical angles.

2. THEORETICAL MODEL

We propose to combine LC material with PSHE to investigate the reflection behavior of a linearly polarized light beam on the LC surface under different temperatures. In optics, the LC can be simply considered as a uniaxial anisotropic medium controlled by the temperature and followed by the derivation of their refractive indices and dielectric constants. By considering the Lorentz-Lorenz formula, the classical Clausius-Mossotti equation gives a relationship among the dielectric constant (ε), molecular polarizability (α), and molecular packing density (N) for the isotropic medium at low frequency [45, 46]:

$$\frac{n^2-1}{n^2+2} = \frac{4\pi}{3} N\alpha. \tag{1}$$

Here, $n = \sqrt{\varepsilon}$ stands for the refractive index in media at optical frequencies, and the magnetic permeability (μ) is chosen as 1.

In 1966, Vuks [47] modified the Lorentz-Lorenz equation and introduced the anisotropic of LC, yielding the following equation:

$$\frac{n_{e,o}^2-1}{\langle n^2\rangle+2} = \frac{4\pi}{3} N\alpha_{e,o}, \tag{2}$$

where n_e and n_o denote the refractive indices of extraordinary and ordinary lights, respectively, both as a function of wavelength and temperature. Based on the Vuks model at a fixed wavelength, the refractive indices of LC can be expressed in terms of the average refractive index and birefringence [48, 49]. The average refractive index defined as $(n_e + 2n_o)/3$ decreases linearly with the increase of temperature, expressed as $\langle n\rangle = A - BT$ [48, 49], and the degree of linearity (A and B) is only related to the LC material properties. We note that the LC birefringence property ($\Delta n = n_e - n_o$) also depends linearly on the order parameter [50]; therefore, the temperature-dependent birefringence can be rewritten based on the Haller's approximation [51]:

$$\Delta n = (\Delta n)_0 \left(1 - \frac{T}{T_c}\right)^{\beta}, \tag{3}$$

where $(\Delta n)_0$ denotes the LC birefringence when $T = 0\,\mathrm{K}$, and the index β is a material constant. Then, the temperature-dependent refractive index of the LC can be obtained when the temperature is below the CP temperature [48, 49, 52]:

$$n_e = \langle n\rangle + \frac{2}{3}\Delta n \approx A - BT + \frac{2}{3}(\Delta n)_0 \left(1 - \frac{T}{T_c}\right)^{\beta}, \tag{4}$$

$$n_o = \langle n\rangle - \frac{1}{3}\Delta n \approx A - BT - \frac{1}{3}(\Delta n)_0 \left(1 - \frac{T}{T_c}\right)^{\beta}, \tag{5}$$

where T denotes the LC temperature, and T_c denotes the CP temperature. We should note that the LC material can be expressed as the average refractive index $\langle n\rangle$ when T is higher than T_c. Considering μ as 1, we can also get the dielectric constants ($\varepsilon_{LC}^e = n_e^2$, $\varepsilon_{LC}^o = n_o^2$, and ε_L) of LC material in the cases of liquid crystal state ($T < T_c$) and liquid state ($T > T_c$), denoted as:

$$\varepsilon_{LC}^e = \left[A - BT + \frac{2}{3}(\Delta n)_0 \left(1 - \frac{T}{T_c}\right)^{\beta}\right]^2, \tag{6}$$

$$\varepsilon_{LC}^o = \left[A - BT - \frac{1}{3}(\Delta n)_0 \left(1 - \frac{T}{T_c}\right)^{\beta}\right]^2. \tag{7}$$

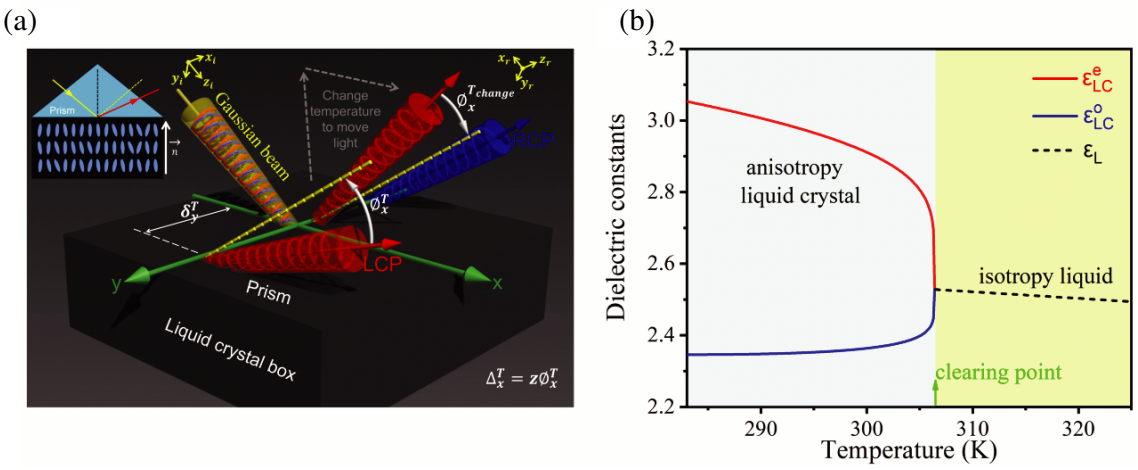

Figure 1. Diagram of LC-based temperature sensing based on the PSHE. Here and below, we consider the incidence of p-polarized wave, and the working wavelength in free space is 589 nm. (a) The spatial and angular shifts at the prism-LC interface. The dielectric constant of prism is $\varepsilon_1 = 4$. The LC molecules inside the box can be considered as a uniaxial anisotropic media with $\bar{\bar{\varepsilon}}_{LC} = \mathrm{diag}(\varepsilon^o_{LC}, \varepsilon^o_{LC}, \varepsilon^e_{LC})$ under (282.9 K $\sim$ 306.39 K) and an isotropic liquid with ε_L under (306.4 K $\sim$ 325 K), where the temperature-dependent dielectric constants ε^o_{LC}, ε^e_{LC}, and ε_L as shown in (b). The average refractive index $\langle n \rangle$ and birefringence Δn of 5CB LC material (4-cyano-4-n-pentylbiphenyl) at $\lambda = 589$ nm can be obtained by choosing the parameters as: $A = 1.7674$, $B = 5.79 \times 10^{-4}\,\mathrm{K}^{-1}$, $(\Delta n)_0 = 0.3505$, $\beta = 0.1889$ [52].

$$\varepsilon_L = [A - BT]^2. \tag{8}$$

We consider a spatially confined light beam incident from the glass prism to a box filled with LC molecules, as shown in Fig. 1(a). At the interface between the prism and LC material, the PSHE happens allowing for the splitting of left- and right-handed circularly polarized (LCP and RCP) components, which leads to the spin spatial and angular shifts. From Eqs. (6) and (7), we can find that the dielectric constants of LC change with the variation of temperature leading to the modulation of PSHE. As shown in the upper left inset of Fig. 1(a), the long axis of the LC molecules tends to be parallel to the pointing vector showing an ordered distribution, i.e., parallel to the z-direction. However, there is always a part of LC molecules whose long axis is not fully parallel to the pointing vector. Therefore, this LC box can be regarded as a uniaxial anisotropic medium $\bar{\bar{\varepsilon}}_{LC} = \mathrm{diag}(\varepsilon_x, \varepsilon_x, \varepsilon_z)$, in which $\varepsilon_x = \varepsilon^o_{LC}$, $\varepsilon_z = \varepsilon^e_{LC}$. To explore the PSHE in this structure, we should deduce the reflection coefficients between the isotropic transparent prism and anisotropic LC, expressed as [53, 54]:

$$r_p = \frac{\varepsilon_x k_z^1 - n_1^2 k_z^e}{\varepsilon_x k_z^1 + n_1^2 k_z^e}, \tag{9}$$

$$r_s = \frac{k_z^1 - k_z^o}{k_z^1 + k_z^o}. \tag{10}$$

Here, k_z^1 is the z-component of wavevector of the isotropic transparent prism; k_z^o and k_z^e are the z-components of wavevectors of ordinary and extraordinary waves, respectively; p and s stand for transverse-magnetic/TM and transverse-electric/TE waves.

In this work, we only consider the incident beam with p-polarized state, and the condition with s-polarized state can be derived in a similar way. For the spin spatial shift, the LCP and RCP components of the reflected light beam will split in the transverse direction (y-direction) with an equal shift, and the physical quantity of spin splitting described here is the transverse spatial shift (δ_y). Taking into account the influence of in-plane wave vectors, the reflection coefficients need to be expanded by first-order Taylor. Then according to the three-dimensional rotation matrix transformation and the center

of gravity formulas, the exact transverse spatial shift of the LCP component can be obtained as [17]:

$$\delta_y = -\frac{k\omega^2(p(p+s)+\rho(\xi+\rho))\cot\theta_i}{\gamma^2+k^2\omega^2(p^2+\rho^2)+\chi^2+((p+s)^2+(\xi+\rho)^2)(\cot\theta_i)^2}. \tag{11}$$

Here, p and ρ are the real and imaginary parts of r_p; s and ξ are the real and imaginary parts of r_s; χ and γ represent the real and imaginary parts of $\partial r_p/\partial\theta_i$. In addition to the spatial shift, the splitting beam also rotates a certain angle around the origin axis, which is related to the angular shift. The angular shift is corresponding to the propagation distance of the reflected beam and is usually much larger than the spatial shift. Here, we consider the angular shift in the in-plane direction (x-direction), and the physical quantity of spin splitting described is the in-plane angular shift (Δ_x). After calculation, the exact in-plane angular shift of the LCP component can be described as [55, 56]:

$$\Delta_x = -\frac{2z(\gamma\rho+p\chi)}{n_1(\gamma^2+k^2\omega^2(p^2+\rho^2)+\chi^2+((p+s)^2+(\xi+\rho)^2)(\cot\theta_i)^2)}, \tag{12}$$

where z is the propagation distance of reflected beam, and n_1 stands for the refractive index of prism. In the following analysis, z is taken as 250 mm.

3. RESULTS AND DISCUSSIONS

Figure 1(b) shows the numerical simulation of the dielectric constants of a widely used commercial 5CB LC material (4-cyano-4-n-pentylbiphenyl) [52]. It can be seen that when the external temperature increases, the dielectric constant parallel to the long-axis of LC molecules (ε^e_{LC}) decreases, while it increases for the direction perpendicular to the long-axis (ε^o_{LC}). As the temperature continues to increase and reach the CP temperature, LC transforms into an isotropic liquid with $\varepsilon_L = \varepsilon^e_{LC} = \varepsilon^o_{LC}$. We can also find that the temperature-gradients ($|d\varepsilon^e_{LC}/dT|$ and $|d\varepsilon^o_{LC}/dT|$) of dielectric constants show a relatively flat variation in a wide-range of temperature while represents a rapid change near the CP. Once the temperature exceeds the CP temperature, the temperature-gradients of dielectric constants synchronously jump abruptly to a stable value and then show a slow linear transformation trend in the high-temperature region. Such unique properties of temperature-gradient in dielectric constants provide a sensitive way for sensing, especially around the CP. It is interesting to note that the photonic spin splitting on anisotropic media is much larger than that on isotropic media due to the joint expression of Pancharatnam-Berry phase and spin redirection Berry phase, resulting in giant PSHE [57–60]. In the following parts, we plan to solve these important questions: 1. Whether the temperature sensitivity can be further improved by detecting the PSHE at CP; 2. Whether the high sensitivity occurs around the CP temperature freely adjustable towards low temperature, which limits the effective LC temperature sensing applications and the active manipulation of PSHE according to the variation of temperature.

By considering the PSHE at the LC surface, we plot the transverse spatial shift versus the incident angle and temperature, as shown in Fig. 2(a). Here, we can find that the spatial shift shows a very large value and rapid variation near the Brewster angle. In the case of fixed incident angle, the transverse spatial shift changes from the positive value to the negative one or vice versa after introducing the tiny perturbation of temperature, which provides a sensitive method for optical sensing. We also analyze the sensitivity of transverse spatial shifts as $S = \left|\frac{\partial\delta_y}{\partial T}\right|$ of this model, as shown in Fig. 2(b). Interestingly, we can reveal that there exists a very large value of sensitivity near the CP temperature.

Then, we take four different incident angles ($\theta_i = 45°, 46°, 47°, 48°$) from Fig. 2(a), and the corresponding transverse spatial shifts and sensitivity are shown in Figs. 2(c) and 2(d). The results show that the range of high sensitivity is significantly shifted to the low temperature direction by increasing the incident angle, which provides a way to achieve high sensitivity over a wide-range of temperature for LC, i.e., obtaining effective temperature sensing by setting the optimal incident angle. In addition, we focus on the four ranges of temperature (302.83 K $\sim$ 304.26 K, 299.71 K $\sim$ 302.06 K, 295.04 K $\sim$ 298.57 K, and 288.64 K $\sim$ 293.54 K) where the transverse spatial shifts change from the maximum value to the minimum one (Fig. 2(c)). We can find that, with the decreasing of incident angle, the variation trend becomes more rapid corresponding to the higher sensitivity, as shown in Fig. 2(d). We can also explore that the sensitivities in the above cases are 7.1λ/K, 9.3λ/K, 13.3λ/K, and 21.1λ/K, respectively.

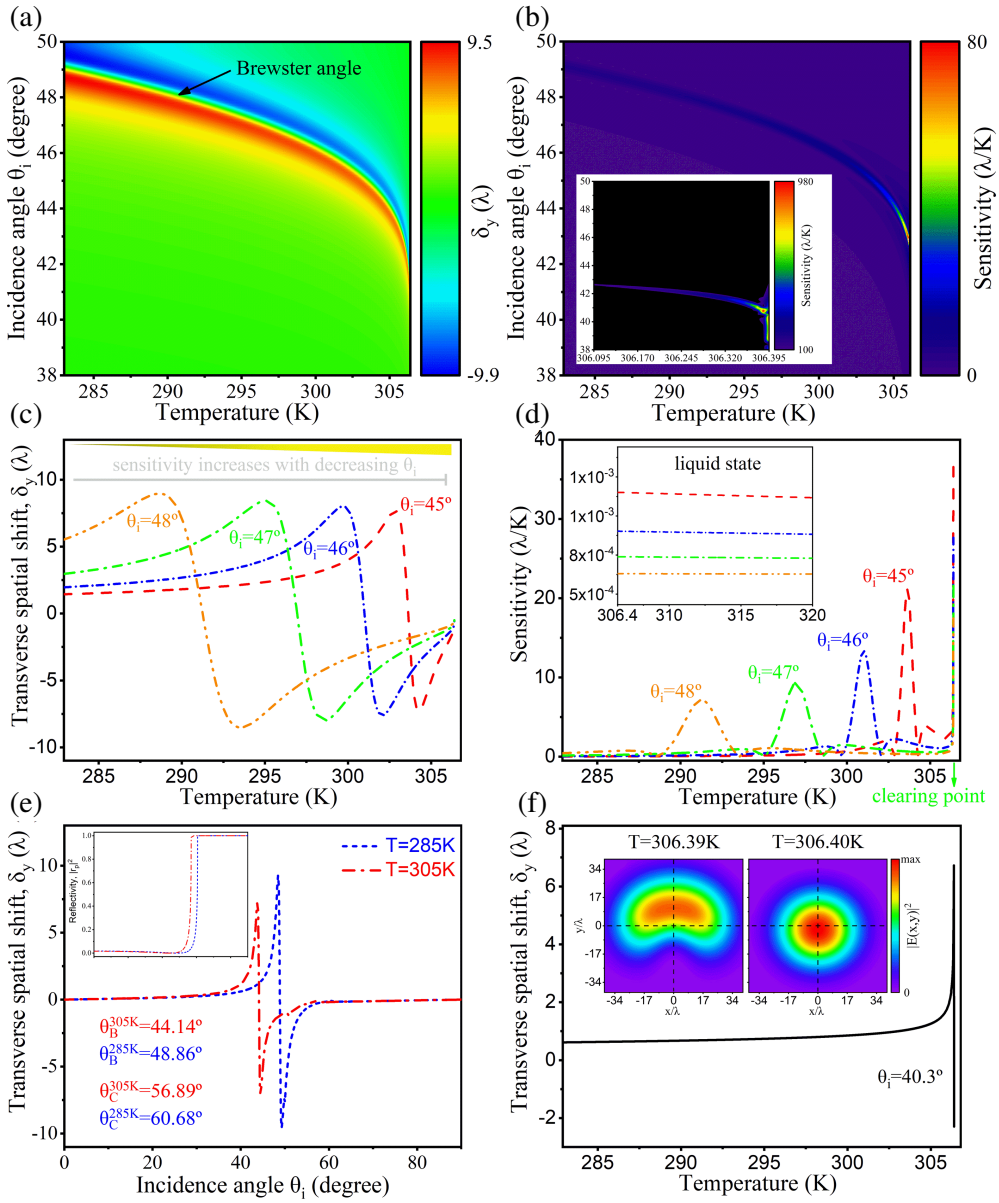

Figure 2. The temperature-dependent transverse spatial shifts (a) and their sensitivity (b) near the Brewster angles. As shown in Eq. (11), the transverse spin shift under p-polarization is mainly affected by the term of $\frac{|r_s|}{|r_p|}$. It can be seen that the near-zero-reflection point ($|r_p| \approx 0$) caused by the Brewster effect enlarges the spin shift greatly and represents a much larger shift than that in other angles. (c) and (d) show the transverse spatial shifts and their sensitivity with temperature at different incidence angles ($\theta_i = 45°, 46°, 47°, 48°$), where the insets show the sensitivity in liquid state ($T > 306.4\,\mathrm{K}$). In order to clearly show the changes at CP, the selection of abscissas for all curves here and next has been expanded to 306.8 K, which is slightly larger than CP temperature. (e) describes the variation of the transverse spatial shifts (δ_y) with the incident angle at different temperatures ($T = 285\,\mathrm{K}$ and $T = 305\,\mathrm{K}$), where the inset shows the reflectivity with different temperatures corresponding to different Brewster angles of LC. (f) shows the transverse spatial shift with varying temperature at incidence angle $\theta_i = 40.3°$, where the insets show the field distributions of the reflected light with the LCP component under $T = 306.39\,\mathrm{K}$ and $T = 306.4\,\mathrm{K}$. Here, the field distributions are obtained by integrating the reflection electric field, and the visualized center of gravity drift is described as a transverse (y-direction) spatial shift. The beam waist is selected as 30λ.

In order to explore why the sensitivity can be modulated under different incident angles, we focus our attention on the special incident angle, namely the Brewster angle. Then, the images of the transverse spatial shifts and reflectivity under $T = 285\,\mathrm{K}$ and $T = 305\,\mathrm{K}$ are plotted in Fig. 2(e). It can be seen that the near-zero reflectivity around the Brewster angle arising from the Brewster effect will result in giant transverse spatial shift, much larger than that under other incidence angles. In addition, the reflectivity curve also shows that the temperature can affect the position of the Brewster angle. Thus, setting the optimal incident angle can be efficiently implemented for temperature sensing. The mechanism of the movement of sensitivity is due to the large and opposite spin shifts near the Brewster angles of near-zero reflectivity ($|r_p|^2 \approx 0$). Here, the Brewster angle is determined only by the dielectric constants of LC which is directly related to the temperature, thus the Brewster angle varies at different temperatures. It means that changing the incident angle will result in a giant spatial shift at a determined temperature much larger than others, bringing the large sensitivity.

Turn our attention to CP, where the transition from liquid crystal state to liquid state happens. Fig. 2(d) shows that the sensitivities corresponding to the above different incident angles are $37.5\lambda/\mathrm{K}$, $27.8\lambda/\mathrm{K}$, $21.8\lambda/\mathrm{K}$, and $18.0\lambda/\mathrm{K}$, which are greater than that in the continuous liquid crystal state. As for the liquid state area beyond the CP temperature, the inset of Fig. 2(d) shows several linear and tiny sensitivities, which are far less than $10^{-3}\lambda/\mathrm{K}$, so we do not think that there is a sensing possibility. The inset of Fig. 2(b) also shows that the maximum sensitivity at CP can even reach $9847\lambda/\mathrm{K}$ ($0.058\,\mathrm{cm/K}$). These results are attributed to the dramatically variable optical state of LC at CP temperature, then the sharp reduction of abnormal spatial shift and huge sensitivity appear. This phenomenon occurs at a wide-range of incident angles for transverse spatial shifts.

Similarly, we can tune the incident angle to the Brewster angle corresponding to the temperature near CP and explore the results with the combination of two mechanisms: Brewster effect and sharp transition in CP, as shown in Fig. 2(f). It is found that the spatial shifts experience a dramatic change when the incident angle is adjusted to 40.3°. The insets of Fig. 2(f) show the light intensity distribution of the LCP component at $T = 306.39\,\mathrm{K}$ and $T = 306.4\,\mathrm{K}$, and the corresponding shifts are $\delta_y^{306.39\,\mathrm{K}} = 6.73\lambda$ and $\delta_y^{306.4\,\mathrm{K}} = -2.29\lambda$. We can see that a tiny temperature change of $0.01\,\mathrm{K}$ also causes a huge change in the transverse spatial shift, which results in a very large sensitivity with $9021\lambda/\mathrm{K}$. We can attribute the above temperature sensing into two regions. The first one is that, by setting the incident angle near a temperature-controlled Brewster angle, the spin shift at the specified temperature is much greater than that at other temperatures, resulting in ultra-high sensitivity. The other is that for CP temperature, there is always a high sensitivity due to the huge temperature-gradient dielectric constant and the drastic changes in the nature of LC.

Note that another spin splitting phenomenon called spin angular shift is much larger than the spatial shift, which will help us to greatly improve the sensitivity. Fig. 3(a) shows the variation of the in-plane angular shifts with the incident angle and temperature, and it indicates that the maximum in-plane angular shift can achieve $\pm 1100\lambda$, which is much larger than the transverse spatial shifts (below 10λ). There exist two abnormal variation regions manifested by giant changes of shifts near both of the Brewster and critical angles, as shown in Fig. 3(b). Importantly, the position of the singular PSHE phenomena can be modulated by varying the temperature ($\theta_B^{285\,\mathrm{K}} = 48.86°$, $\theta_B^{305\,\mathrm{K}} = 44.14°$, $\theta_C^{285\,\mathrm{K}} = 60.68°$, $\theta_C^{305\,\mathrm{K}} = 56.89°$), providing one more sensitive region compared with the transverse spatial shift. When the incident angle exceeds the critical angle, the in-plane angular shifts will suddenly become zero and can be maintained with increasing temperature. Thus, it can be expected that the high sensitivity at CP appears near the varying critical angles.

Then we consider the determined temperature-dependent Brewster and critical angles, respectively, as shown in Figs. 3(c) and 3(d). Their corresponding sensitivities are shown in Figs. 3(e) and 3(f), respectively. At first we set the incident angle near the Brewster angle, and it is clearly found that the sensitivities are improved by two orders of magnitude compared to that in the transverse spatial shifts. With an incident angle of 40.3° (Fig. 3(e)), the temperature change of $0.01\,\mathrm{K}$ makes a huge change in the in-plane angular shift from $\Delta_x^{306.39\,\mathrm{K}} = 1004.5\lambda$ to $\Delta_x^{306.4\,\mathrm{K}} = -400.4\lambda$, and the corresponding sensitivity reaches a giant value of $140484\lambda/\mathrm{K}$ ($8.27\,\mathrm{cm/K}$). Comparatively, we improve the temperature sensitivity by one order of magnitude over the previous method [15] where the authors have reported the temperature sensor based on the surface plasmon resonance and Goos-Hänchen shifts, and the maximum temperature sensitivity is about $0.79\,\mathrm{cm/K}$. Additionally, we consider using the critical angle

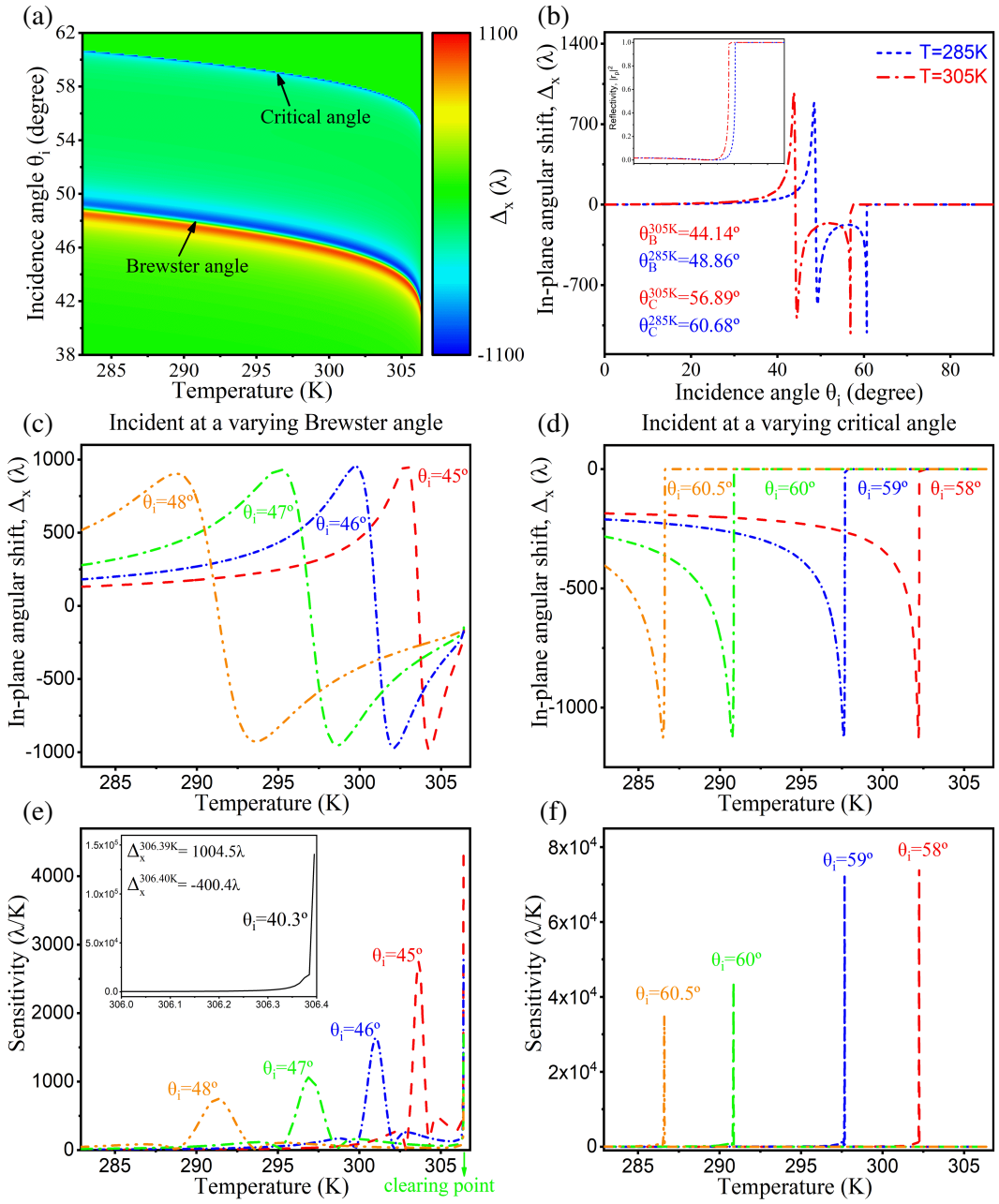

Figure 3. (a) The temperature-dependent in-plane angular shifts near the varying Brewster and critical angles. (b) shows the variation of the in-plane angular shifts (Δ_x) with the incident angle at different temperatures ($T = 285\,\mathrm{K}$ and $T = 305\,\mathrm{K}$), where the inset shows the reflectivity. Here, different temperatures correspond to different Brewster and critical angles. (c) and (e) show the in-plane angular shifts and their sensitivity with temperature change at different incidence angles ($\theta_i = 45°, 46°, 47°, 48°$), where the inset represents the image of the sensitivity of $\theta_i = 40.3°$. (d) and (f) describe the in-plane angular shifts and their sensitivity with temperature change at different incidence angles ($\theta_i = 58°, 59°, 60°, 60.5°$). The beam waist is selected as 30λ.

to achieve the high sensitivity in the range relatively far away from the CP temperature and find that the corresponding sensitivity trend still increases with the decrease of incident angles. Here it is shown that the sensitivity can reach about 35410λ/K (2.09 cm/K), 44153λ/K (2.6 cm/K), 72149λ/K (4.2 cm/K),

and 74384λ/K (4.4 cm/K) at different incidence angles $\theta_i = 58°, 59°, 60°, 60.5°$. This allows us to achieve a wide-range ultra-high temperature sensitivity through flexibly selecting the incidence angle.

Finally, we discuss other kinds of potential methods for further improving the sensitivity. The first one is from the spin shifts, such as increasing the beam waist and using weak measurement techniques [18, 61]. The other one is from the LC material, and we can introduce those with larger temperature-gradient dielectric constant. Here we take the transverse spatial shifts as an example, and the in-plane angular shifts can be analyzed in a similar way. Fig. 4(a) shows the significant and nearly linear amplification effect of the beam waist on the spin shifts near the Brewster angle, which can be expected to have similar amplification effect on the temperature sensitivity. When the beam waist is large enough, the sensitivity near Brewster angle will even exceed that near CP point, as shown in Fig. 4(c). It is important that such a result does not break the ultra-high sensitivity near the CP temperature, and it still exists. According to Fig. 4(a), because the amplification effect of the beam waist on the transverse spin shifts is mainly reflected near Brewster angle, which has little effect on other incident angles, a higher sensitivity than CP temperature is achieved at the temperature corresponding to Brewster angle, which also shows that the beam waist can also flexibly adjust the size and position of sensitivity. Here, it is suggested that we can obtain a large value sensitivity by flexibly choosing the beam waist for practical experiment. Further, we can also enhance the sensitivity of temperature sensor by performing the PSHE on different LC materials [52], where UCF series LC materials have lower cross-over temperatures and a wider temperature range of LC states relative to CB series. The

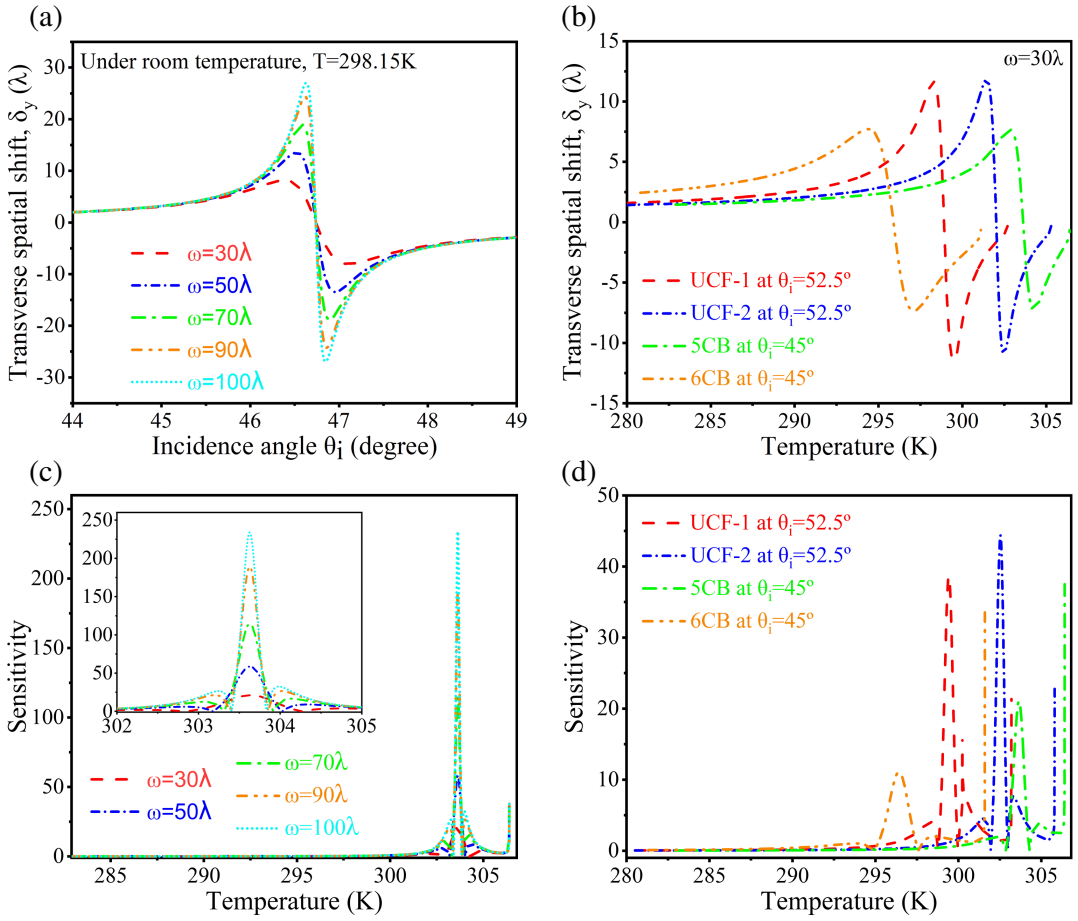

Figure 4. (a) shows the effect of beam waist on the transverse spatial shifts and under room temperature ($T = 298.15$ K). (b) and (d) show the effect of different types of LC materials (UCF-1, UCF-2, 5CB, 6CB) on the transverse spatial shifts and their sensitivity at $\omega = 30\lambda$. (c) shows the effect of beam waist on the sensitivity at $\theta_i = 45°$ under room temperature.

greater birefringence describes a more intense degree of anisotropy, corresponding to a larger spin shift ($\delta_{\max}^{\mathrm{UCF}} > \delta_{\max}^{\mathrm{CB}}$), as shown in Fig. 4(b). In addition, according to [52], the UCF series LC has a larger temperature-gradient dielectric constant ($\left|d\varepsilon_{LC}^{e,o}/dT\right|_{\mathrm{UCF}} > \left|d\varepsilon_{LC}^{e,o}/dT\right|_{\mathrm{CB}}$); therefore, it can be expected that the UCF series LC material can further improve the sensitivity of temperature sensing, as shown in Fig. 4(d).

4. CONCLUSION

In summary, we have investigated the spin spatial and angular shifts in photonic spin Hall effect (PSHE) when the linearly polarized light beam is reflected at the prism-liquid crystal (LC) material interface. We have explored that using the temperature-dependent properties of LC allows for realizing an ultra-highly sensitive temperature sensor, where the sensitivity is much better than the conventional one. The physical mechanism of this interesting phenomenon is that the spin spatial and angular shifts have shown a very rapid variation near the Brewster and critical angles by applying very tiny change of temperature. We have also revealed that, when the system state is close to the clearing point (CP), a great sensitivity of this temperature sensor can be achieved. These findings not only provide an active way for manipulating the PSHE but also extend the spin-orbit interaction for developing spin-based nanophotonic devices.

ACKNOWLEDGMENT

X.Z. was supported by the National Natural Science Foundation of China (11604095) and the Training Program for Excellent Young Innovators of Changsha (kq2107013).

REFERENCES

1. Wade, S. A., S. F. Collins, and G. W. Baxter, "Fluorescence intensity ratio technique for optical fiber point temperature sensing," *J. Appl. Phys.*, Vol. 94, 4743–4756, 2003.
2. Li, E., X. Wang, and C. Zhang, "Fiber-optic temperature sensor based on interference of selective higher-order modes," *Appl. Phys. Lett.*, Vol. 89, 091119, 2006.
3. Choi, H. Y., K. S. Park, S. J. Park, U. C. Paek, B. H. Lee, and E. S. Choi, "Miniature fiber-optic high temperature sensor based on a hybrid structured Fabry-Perot interferometer," *Opt. Lett.*, Vol. 33, 2455–2457, 2008.
4. Ramakrishnan, M., G. Rajan, Y. Semenova, and G. Farrell, "Overview of fiber optic sensor technologies for strain/temperature sensing applications in composite materials," *Sensors*, Vol. 16, 99, 2016.
5. Pérez-García, G. F., J. L. Camas-Anzueto, G. Anzueto-Sánchez, M. Pérez-Patricio, and F. R. López-Estrada, "Demonstration of improving the sensitivity of a fiber optic temperature sensor using the wavelength of maximum absorption of the lophine," *Measurement*, Vol. 187, 110378, 2022.
6. Song, E., M. Chen, Z. Chen, et al., "Mn^{2+}-activated dual-wavelength emitting materials toward wearable optical fibre temperature sensor," *Nat. Commun.*, Vol. 13, 1–9, 2022.
7. Moreira, M. F., et al., "Cholesteric liquid-crystal laser as an optic fiber-based temperature sensor," *Appl. Phys. Lett.*, Vol. 85, 2691–2693, 2004.
8. Zhao, L., Y. Wang, Y. Yuan, et al., "Whispering gallery mode laser based on cholesteric liquid crystal microdroplets as temperature sensor," *Opt. Commun.*, Vol. 402, 181–185, 2017.
9. Wang, F., Y. Liu, Y. Lu, L. Zhang, J. Ma, L. Wang, and W. Sun, "High-sensitivity Fabry-Perot interferometer temperature sensor probe based on liquid crystal and the Vernier effect," *Opt. Lett.*, Vol. 43, 5355–5358, 2018.
10. Chiang, L. Y., C. T. Wang, T. S. Lin, S. Pappert, and P. Yu, "Highly sensitive silicon photonic temperature sensor based on liquid crystal filled slot waveguide directional coupler," *Opt. Express*, Vol. 28, 29345–29356, 2020.

11. Chen, C., W.-C. Lin, L.-S. Liao, et al., "Optical temperature sensing based on the Goos-Hänchen effect," *Appl. Opt.*, Vol. 46, 5347–5351, 2007.
12. Tang, T., C. Li, L. Luo, Y. Zhang, and Q. Yuan, "Thermo-optic Imbert-Fedorov effect in a prism-waveguide coupling system with silicon-on-insulator," *Opt. Commun.*, Vol. 370, 49–54, 2016.
13. Turhan-Sayan, G., "Temperature effects on surface plasmon resonance: Design considerations for an optical temperature sensor," *J. Lightwave Technol.*, Vol. 21, 805, 2003.
14. Chen, C. W., H. P. Chiang, D. P. Tsai, and P. T. Leung, "Temperature dependence of the surface-plasmon-induced Goos-Hänchen shifts," *Appl. Phys. B*, Vol. 107, 111–118, 2012.
15. Xu, Y., L. Wu, and L. K. Ang, "Ultrasensitive optical temperature transducers based on surface plasmon resonance enhanced composited Goos-Hänchen and Imbert-Fedorov shifts," *IEEE J. Sel. Top. Quantum Electron.*, Vol. 27, 1–8, 2021.
16. Onoda, M., S. Murakami, and N. Nagaosa, "Hall effect of light," *Phys. Rev. Lett.*, Vol. 93, 083901, 2004.
17. Bliokh, K. Y. and Y. P. Bliokh, "Conservation of angular momentum, transverse shift, and spin Hall effect in reflection and refraction of an electromagnetic wave packet," *Phys. Rev. Lett.*, Vol. 96, 073903, 2006.
18. Hosten, O. and P. Kwiat, "Observation of the spin Hall effect of light via weak measurements," *Science*, Vol. 319, 787–790, 2008.
19. Bliokh, K. Y., A. Niv, V. Kleiner, and E. Hasman, "Geometrodynamics of spinning light," *Nat. Photon.*, Vol. 2, 748, 2008.
20. Qin, Y., Y. Li, H. He, and Q. Gong, "Measurement of spin Hall effect of reflected light," *Opt. Lett.*, Vol. 34, 2551, 2009.
21. Ling, X., X. Zhou, K. Huang, and Y. Liu, "Recent advances in the spin Hall effect of light," *Rep. Prog. Phys.*, Vol. 80, 066401, 2017.
22. Kim, M., D. Lee, and J. Rho, "Spin Hall effect: Spin Hall effect under arbitrarily polarized or unpolarized light," *Laser Photonics Rev.*, Vol. 15, 7, 2021.
23. Petersen, J., J. Volz, and A. Rauschenbeutel, "Chiral nanophotonic waveguide interface based on spin-orbit interaction of light," *Science*, Vol. 34, 67–71, 2014.
24. Bliokh, K. Y., F. J. Rodríguez-Fortuño, F. Nori, and A. V. Zayats, "Spin-orbit interactions of light," *Nat. Photon.*, Vol. 9, 796, 2015.
25. Cardano, F. and L. Marrucci, "Spin-orbit photonics," *Nat. Photon.*, Vol. 9, 776, 2015.
26. Shao, Z., J. Zhu, Y. Chen, Y. Zhang, and S. Yu, "Spin-orbit interaction of light induced by transverse spin angular momentum engineering," *Nat. Commun.*, Vol. 9, 1–11, 2018.
27. Fu, S., C. Guo, G. Liu, Y. Li, H. Yin, Z. Li, and Z. Chen, "Spin-orbit optical Hall effect," *Phys. Rev. Lett.*, Vol. 123, 243904, 2019.
28. Fang, L., H. Wang, Y. Liang, H. Cao, and J. Wang, "Spin-orbit mapping of light," *Phys. Rev. Lett.*, Vol. 127, 233901, 2021.
29. Chi, C., Q. Jiang, Z. Liu, L. Zheng, M. Jiang, H. Zhang, F. Lin, B. Shen, and Z. Fang, "Selectively steering photon spin angular momentum via electron-induced optical spin Hall effect," *Sci. Adv.*, Vol. 7, eabf8011, 2021.
30. Zhou, X., Z. Xiao, H. Luo, and S. Wen, "Experimental observation of the spin Hall effect of light on a nanometal film via weak measurements," *Phys. Rev. A*, Vol. 85, 043809, 2012.
31. Mi, C., S. Chen, X. Zhou, K. Tian, H. Luo, and S. Wen, "Observation of tiny polarization rotation rate in total internal reflection via weak measurements," *Photonics Res.*, Vol. 5, 92–96, 2017.
32. Wang, B., K. Rong, E. Maguid, V. Kleiner, and E. Hasman, "Probing nanoscale fluctuation of ferromagnetic meta-atoms with a stochastic photonic spin Hall effect," *Nat. Nanotechnol.*, Vol. 15, 450–456, 2020.
33. Wang, R., J. Zhou1, K. Zeng, et al., "Ultrasensitive and real-time detection of chemical reaction rate based on the photonic spin Hall effect," *Apl. Photonics*, Vol. 5, 016105, 2020.

34. Li, S., Z. Chen, L. Xie, Q. Liao, X. Zhou, Y. Chen, and X. Lin, "Weak measurements of the waist of an arbitrarily polarized beam via in-plane spin splitting," *Opt. Express*, Vol. 29, 8777–8785, 2021.
35. Zhou, X., L. Sheng, and X. Ling, "Photonic spin Hall effect enabled refractive index sensor using weak measurements," *Sci. Rep.*, Vol. 8, 1–8, 2018.
36. Zhu, W., H. Xu, J. Pan, et al., "Black phosphorus terahertz sensing based on photonic spin Hall effect," *Opt. Express*, Vol. 28, 25869–25878, 2020.
37. Nie, P., L. Sheng, L. Xie, Z. Chen, X. Zhou, Y. Chen, and X. Lin, "Gas sensing near exceptional points," *J. Phys. D*, Vol. 54, 254001, 2021.
38. Liu, S., X. Yin, and H. Zhao, "Dual-function photonic spin Hall effect sensor for high-precision refractive index sensing and graphene layer detection," *Opt. Express*, Vol. 30, 31925–31936, 2022.
39. Zhou, J., H. Qian, G. Hu, H. Luo, S. Wen, and Z. Liu, "Broadband photonic spin Hall meta-lens," *ACS Nano*, Vol. 12, 82–88, 2018.
40. Du, L., et al., "On-chip photonic spin Hall lens," *ACS Photonics*, Vol. 6, 1840–1847, 2019.
41. Jin, R., L. Tang, J. Li, J. Wang, Q. Wang, Y. Liu, and Z. G. Dong, "Experimental demonstration of multidimensional and multifunctional metalenses based on photonic spin hall effect," *ACS Photonics*, Vol. 7, 512–518, 2020.
42. Xie, Z., T. Lei, H. Qiu, Z. Zhang, H. Wang, and X. Yuan, "Broadband on-chip photonic spin Hall element via inverse design," *Photonics Res.*, Vol. 8, 121–126, 2020.
43. He, A., Y. Xu, B. Gao, T. Zhang, and J. Zhang, "Subwavelength broadband photonic spin hall devices via optical slot antennas," *Laser Photonics Rev.*, Vol. 15, 2000460, 2021.
44. Lei, T., C. Zhou, D. Wang, et al., "On-chip high-speed coherent optical signal detection based on photonic spin-Hall effect," *Laser Photonics Rev.*, Vol. 16, 2100669, 2022.
45. Jackson, J. D., *Classical Electrodynamics*, Wiley, New York, 1962.
46. Kong, J. A., *Electromagnetic Wave Theory*, EMW Publishing, Cambridge, MA, 2008.
47. Vuks, M. F., "Determination of the optical anisotropy of aromatic molecules from the double refraction of crystals," *Opt. Spectrosc.*, Vol. 20, 361, 1966.
48. Li, J. and S. T. Wu, "Extended Cauchy equations for the refractive indices of liquid crystals," *J. Appl. Phys.*, Vol. 95, 896–901, 2004.
49. Li, J., S. Gauza, and S. T. Wu, "Temperature effect on liquid crystal refractive indices," *J. Appl. Phys.*, Vol. 96, 19–24, 2004.
50. Wu, S. T., "Birefringence dispersions of liquid crystals," *Phys. Rev. A*, Vol. 33, 1270, 1986.
51. Haller, I., "Thermodynamic and static properties of liquid crystals," *Prog. Solid State Chem.*, Vol. 10, 103–118, 1975.
52. Li, J., S. Gauzia, and S. T. Wu, "High temperature-gradient refractive index liquid crystals," *Opt. Express*, Vol. 12, 2002–2010, 2004.
53. Luo, H., W. Hu, X. Yi, H. Liu, and J. Zhu, "Amphoteric refraction at the interface between isotropic and anisotropic media," *Opt. Commun.*, Vol. 254, 353–360, 2005.
54. Shah, S., X. Lin, L. Shen, M. Renuka, B. Zhang, and H. Chen, "Interferenceless polarization splitting through nanoscale van der Waals heterostructures," *Phys. Rev. Appl.*, Vol. 10, 034025, 2018.
55. Aiello, A., M. Merano, and J. P. Woerdman, "Duality between spatial and angular shift in optical reflection," *Phys. Rev. A*, Vol. 80, 061801, 2009.
56. Zhou, X., L. Xie, X. Ling, S. Cheng, Z. Zhang, H. Luo, and H. Sun, "Large in-plane asymmetric spin angular shifts of a light beam near the critical angle," *Opt. Lett.*, Vol. 44, 207–210, 2019.
57. Ling, X., X. Zhou, X. Yi, et al., "Giant photonic spin Hall effect in momentum space in a structured metamaterial with spatially varying birefringence," *Light: Sci. Appl.*, Vol. 4, e290, 2015.
58. Ling, X., F. Guan, X. Cai, et al., "Topology-induced phase transitions in spin-orbit photonics," *Laser Photonics Rev.*, Vol. 15, 2000492, 2021.
59. Ling, X., W. Xiao, S. Chen, X. Zhou, H. Luo, and L. Zhou, "Revisiting the anomalous spin-Hall effect of light near the Brewster angle," *Phys. Rev. A*, Vol. 103, 033515, 2021.

60. Mazanov, M., O. Yermakov, A. Bogdanov, and A. Lavrinenko, "On anomalous optical beam shifts at near-normal incidence," *APL Photonics*, Vol. 7, 101301, 2022.
61. Neugebauer, M., S. Nechayev, M. Vorndran, G. Leuchs, and P. Banzer, "Weak measurement enhanced spin Hall effect of light for particle displacement sensing," *Nano Lett.*, Vol. 19, 422, 2019.